Colloids and Surfaces A: Physicochemical and Engineering Aspects 721 (2025) 137214

Contents lists available at ScienceDirect

Colloids and Surfaces A: Physicochemical and Engineering Aspects

journal homepage: www.elsevier.com/locate/colsurfa

# Construction of malononitrile-functionalized conjugated microporous polymers as adsorbents for effective adsorption of Rhodamine B and density functional theory perspective

Mohamed Gamal Mohamed [a,b,*], Ahmed M. Elewa [c,**], Nian-Ping Chen [a], Ahmed A.K. Mohammed [b], Shiao-Wei Kuo [a,d,*]

[a] Department of Materials and Optoelectronic Science, Center for Functional Polymers and Supramolecular Materials, National Sun Yat-Sen University, Kaohsiung 804, Taiwan
[b] Chemistry Department, Faculty of Science, Assiut University, Assiut 71515, Egypt
[c] Department of Chemical Engineering, National Tsing Hua University, Hsinchu 300044, Taiwan
[d] Department of Medicinal and Applied Chemistry, Kaohsiung Medical University, Kaohsiung 807, Taiwan

## GRAPHICAL ABSTRACT

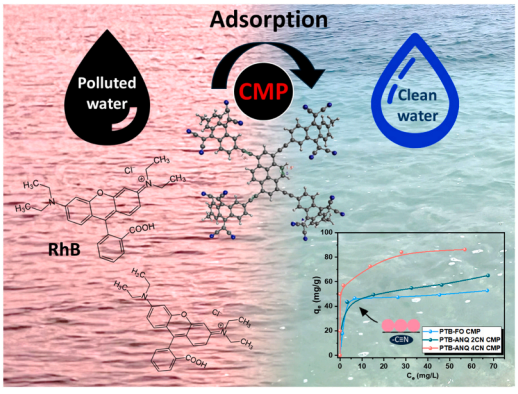


## ARTICLE INFO

*Keywords:*
Pyrene
Anthraquinone
Conjugated microporous polymers
Dye adsorption
Rhodamine B

## ABSTRACT

The escalating challenges of water pollution, driven by rapid industrialization and population growth, necessitate innovative solutions for removing hazardous contaminants such as synthetic dyes. Rhodamine B (RhB), a prevalent pollutant in wastewater, poses significant environmental and human health risks due to its toxicity and persistence. Conjugated microporous polymers (CMPs) have emerged as promising adsorbents for dye removal owing to their high surface area, tunable porosity, and versatile functionalization. In this study, we synthesized and characterized three CMPs [PTB-FO CMP, PTB-ANQ 2CN CMP, and PTB-ANQ 4CN CMP] differing in cyano group content and systematically evaluated their RhB adsorption performance under varying conditions and

* Corresponding authors at: Department of Materials and Optoelectronic Science, Center for Functional Polymers and Supramolecular Materials, National Sun Yat-Sen University, Kaohsiung 804, Taiwan.
** Corresponding author.
*E-mail addresses:* mgamal.eldin12@aun.edu.eg (M.G. Mohamed), ahmed.m.elawa@gmail.com (A.M. Elewa), kuosw@faculty.nsysu.edu.tw (S.-W. Kuo).

https://doi.org/10.1016/j.colsurfa.2025.137214
Received 30 March 2025; Received in revised form 2 May 2025; Accepted 13 May 2025
Available online 14 May 2025

contact times. Among these, PTB-ANQ 4CN CMP exhibited the highest adsorption capacity across a broad pH range, demonstrating superior stability and enhanced dye-polymer interactions facilitated by cyano functionalities. Adsorption kinetics followed a pseudo-second-order model, indicative of a chemisorption-dominated process, while equilibrium adsorption data were best described by the Langmuir isotherm, suggesting monolayer adsorption. Density Functional Theory (DFT) calculations revealed that the calculated ΔN values for electron transfer from the dye to PTB-ANQ 4CN CMP, PTB-ANQ 2CN CMP, and PTB-FO CMP are 0.31, 0.26, and 0.05, respectively. These results indicate that PTB-ANQ 4CN CMP and PTB-ANQ 2CN CMP possess markedly stronger electronic interactions with the dye molecules compared to PTB-FO CMP. Based on the density functional theory (DFT) calculations, the calculated ΔN values for electron transfer from the dye to PTB-ANQ 4CN CMP, PTB-ANQ 2CN CMP, and PTB-FO CMP are 0.31, 0.26, and 0.05, respectively. Notably, PTB-ANQ 4CN CMP and PTB-ANQ 2CN CMP exhibit significantly stronger interactions with dye than PTB-FO CMP. These findings highlight the potential of cyano-functionalized CMPs as effective and sustainable materials for wastewater treatment, offering a viable strategy for mitigating synthetic dye pollution.

## 1. Introduction

Rapid industrialization and population expansion have exacerbated global water pollution, making it one of the most critical environmental challenges of the modern era [1–7]. Of particular concern is the contamination of water bodies by hazardous synthetic chemicals, which pose severe risks to both ecological systems and human health [8]. Among these contaminants, artificial dyes are a major class of pollutants, with nearly 100,000 commercially available variants and an estimated annual production of approximately 700,000 tonnes [9,10]. Alarmingly, around 2 % of these dyes are directly discharged into wastewater streams, contributing to persistent aquatic pollution [11,12]. Industrial sectors such as textiles, paper production, and cosmetics manufacturing are primary contributors to dye effluents, leading to the widespread occurrence of these pollutants in water systems [13,14]. Rhodamine B (RhB), a xanthene-based synthetic dye known for its intense coloration and strong fluorescence properties, is particularly problematic due to its extensive use and environmental persistence [15–18]. Beyond its aesthetic impact on water bodies, RhB is a recognized toxicant with carcinogenic and mutagenic potential, posing substantial risks to aquatic ecosystems and human health [19–22]. Consequently, the efficient removal of RhB from aqueous environments is imperative to mitigate its ecological and public health hazards [23–27].

Extensive research efforts have been dedicated to developing advanced wastewater treatment technologies to safeguard water quality and ensure a sustainable clean water supply. Among various treatment approaches, adsorption has emerged as one of the most effective methods for dye removal due to its operational simplicity, cost efficiency, and high removal efficiency [28–32]. This process relies on the accumulation of dye molecules onto the surface of an adsorbent, making it a versatile and widely adopted technique in wastewater treatment. Over the past few decades, significant progress has been made in developing inorganic and organic adsorbents for removing synthetic dyes and heavy metals from aqueous environments [30–45]. Despite these advancements, many inorganic adsorbents suffer from inherent limitations, including low adsorption capacity, limited surface area, and insufficient long-term stability. Consequently, the development of next-generation inorganic adsorbents with enhanced adsorption performance, structural stability, and recyclability remains a critical challenge in the field of wastewater treatment.

In recent years, organic polymers have attracted considerable attention as versatile adsorbents for wastewater treatment. Various classes of polymer-based materials, including conjugated linear polymers [39], porous polymers [1], metal-organic frameworks (MOFs) [46–48] and covalent organic frameworks (COFs) [49,50] have demonstrated significant potential owing to their cost-effectiveness, tunable structures, and favorable photophysical properties. Among these, conjugated microporous polymers (CMPs) have emerged as particularly promising candidates for wastewater remediation [51–54] and photocatalytic $H_2$ production [55–58]. CMPs offer several intrinsic advantages, including an extended π-conjugated network that promotes π–π interactions with organic pollutants, a highly porous framework that facilitates efficient mass transfer in aqueous environments, and a high surface area conducive to enhanced adsorption [59–66]. Furthermore, CMPs can be synthesized via diverse methodologies, allowing for precise structural design and functionalization to optimize their adsorption capacity, selectivity, and reusability [67–74]. CMPs are synthesized from rationally designed monomers, enabling precise control over their pore size, surface area, and chemical functionality—features that are difficult to achieve with conventional adsorbents such as activated carbon or natural zeolites. CMPs often exhibit exceptionally high BET surface areas, comparable to or even surpassing those of activated carbon, which contributes to their high adsorption capacities. Furthermore, their extended π-conjugated networks facilitate strong π–π interactions with aromatic organic pollutants (e.g., dyes), enhancing selective adsorption. Notably, CMPs constructed with robust covalent linkages (e.g., C–C or C–N bonds) offer outstanding thermal and chemical stability, maintaining structural integrity under harsh environmental conditions where some polymer resins or modified zeolites may degrade. These attributes position CMPs as next-generation materials for the efficient and sustainable removal of contaminants from wastewater. The adsorption efficiency of polymers for RhB removal from aqueous solutions is governed by multiple factors, including surface area, porosity, functional group composition, and adsorption process parameters such as pH, temperature, and contact time. A comprehensive understanding of the molecular interactions between RhB and the polymer surface is crucial for optimizing adsorption performance and developing next-generation adsorbents with enhanced efficiency. While various CMPs have been explored for RhB removal [75,76], the specific role of cyano functional groups in influencing adsorption behavior remains unexplored. Given the strong electron-withdrawing nature of cyano groups and their potential to enhance dye-polymer interactions, investigating their impact on RhB adsorption is essential for advancing the design of high-performance adsorbent materials.

In this study, we investigate the influence of cyano group content on the adsorption efficiency of CMPs for dye removal. To achieve this, we successfully synthesized three CMPs: PTB-FO CMP [lacking CN groups], PTB-ANQ 2CN CMP, and PTB-ANQ 4CN CMP incorporating different ratios of cyano functional groups via the Sonogashira polymerization reaction of 1,3,6,8-tetraethynylpyrene (PTB) as a main building unit with three different brominated monomers such as 2,7-dibromo-9-fluorenone (FO-2Br), 2-(2,6-dibromo-10-oxoanthracen-9(10 H)-ylidene) malononitrile (ANQ-2CN 2Br) and 2,2′-(2,6-dibromoanthracene-9,10-diylidene)dimalononitrile (ANQ-4CN 2Br); respectively. The adsorption performance of these CMPs was systematically evaluated using Rhodamine B as a model dye, focusing on elucidating the adsorption mechanisms. Dye adsorption experiments revealed that PTB-ANQ 4CN CMP exhibits a high dye uptake capacity of 90 mg/g, attributed to its large surface area (465 $m^2$/g) and total pore volume (0.4024 $cm^3$/g). Complementary DFT calculations showed that the electron transfer values (ΔN) from RhB to PTB-ANQ 4CN CMP, PTB-ANQ 2CN CMP, and PTB-FO

CMP were 0.31, 0.26, and 0.05, respectively. These findings suggest that PTB-ANQ 4CN CMP and PTB-ANQ 2CN CMP engage in significantly stronger electronic interactions with dye molecules compared to PTB-FO CMP. This research aims to advance the development of efficient and sustainable adsorbents for wastewater treatment, contributing to the broader field of environmental remediation.

## 2. Materials and methods

### 2.1. Materials

All chemicals including 2,6-diaminoanthraquinone (ANQ-2$NH_2$), trimethylsilylacetylene (TMS, 98 %), anthraquinone (ANQ), sodium sulphite ($Na_2SO_3$), malononitrile, titanium(IV) chloride ($TiCl_4$), pyridine, pyrene, nitrobenzene, fluorenone (FO), bromine ($Br_2$), hydrochloric acid (HCl), ethanol (EtOH), Tetrakis(triphenylphosphine) palladium(0) [$Pd(PPh_3)_4$], triphenylphosphine ($PPh_3$), copper(I) iodide (CuI), triethylamine ($Et_3N$), toluene and potassium carbonate ($K_2CO_3$) were ordered from Cross, and Sigma-Aldrich. The supporting information file includes a concise description of the synthesis process for 2,6-dibromoanthracene-9,10-dione (ANQ-$Br_2$) and 1,3,6,8-tetraethynylpyrene (PTB) [77–80].

### 2.2. Synthesis of FO-2Br

Neat $Br_2$ (3.6 mL, 69.4 mmol) was added dropwise to a solution of FO (2.5 g, 13.85 mmol) in $H_2O$ (35 mL) at 0 °C over 20 minutes. The reaction mixture was then heated to 85 °C and stirred for 16 h. After cooling to room temperature, 75 mL of $H_2O$ and 75 mL of saturated $Na_2SO_3$ solution were added. The resulting solid was collected by filtration, washed with water, and dried to yield a yellow product (4.7 g, Scheme S1). FTIR ($cm^{-1}$): 3066.4 (aromatic C-H for FO unit); 1725 (C═O); 1592, 536 (C-Br) [Figure S1]. $^1$H NMR (δ): 7.73, 7.59, 7.35 ppm [Figure S2]. $^{13}$C NMR (δ): 191 (C═O), 142.27, 137.35, 135.29, 127.72, 123.62, 121.89 ppm [Figure S3].

### 2.3. Synthesis of ANQ-2CN 2Br and ANQ-4CN 2Br

A mixture of ANQ-$Br_2$ (1.5 g, 0.55 mmol) and malononitrile (0.44 g, 0.9 mmol) was dissolved in chloroform (150 mL) and stirred while cooling at 0–5 °C. $TiCl_4$ (1.35 mL, 0.9 mmol) was then added dropwise using a dropper, followed by the slow addition of pyridine (1.125 mL, 2.8 mmol) via syringe. The reaction mixture was refluxed for 2 days. After completion, 30 mL of 10 % HCl was added to the flask, and the mixture was filtered to remove the liquid. The filtrate was then extracted with water and chloroform, and the organic layer was collected. The resulting solid was obtained by rotary evaporation and further purified by column chromatography using n-hexane and ethyl acetate (EA0, yielding two distinct powdered products [ANQ-2CN 2Br as an orange powder (Yield: 55 %) and ANQ-4CN 2Br as a red solid (Yield: 45 %), Scheme S2]. For ANQ-2CN 2Br: FTIR ($cm^{-1}$): 3076.72 (aromatic C-H for ANQ unit), 2224.46 (CN), 1676.64 (C═O), 1571.71, 530.32 (C-Br) [Figure S4]. $^{13}$C NMR (δ): 157.5 (C═O), 135, 131.8, 130.1, 129.14, 125.4, 113.4 (CN), 84.3 [Figure S5]. For ANQ-4CN 2Br: FTIR ($cm^{-1}$): 3061.56 (C-H for ANQ unit), 2239.1 (CN); 1561.33 (C═C) [Figure S6]. $^1$H NMR (δ): 8.37, 8.1, 7.89 ppm [Figure S7]. $^{13}$C NMR (δ): 135, 131.8, 130.1, 129, 125.8, 113.5 (CN). 84.4 ppm [Figure S8].

### 2.4. Synthesis of PTB-FO, PTB-ANQ 2CN, and PTB-ANQ 4CN CMPs

PTB (3 mmol) and FO-2Br (6 mmol) or ANQ-2CN 2Br (6 mmol) or ANQ-4CN 2Br (6 mmol), CuI (0.03 g), $PPh_3$ (0.08 g), and $Pd(PPh_3)_4$ (0.07 g) were inserted into a 50 mL Schlenk flask with DMF (25 mL) and $Et_3N$ (25 mL). The reactions were going under 100 °C for 3 days. The resulting solids underwent Soxhlet extraction using THF and MeOH. The collected residue was subsequently dried at 100 °C for 24 h, yielding PTB-FO, PTB-ANQ 2CN, and PTB-ANQ 4CN CMPs as reddish-brown powder. The elemental analysis data for PTB-FO CMP, PTB-ANQ 2CN CMP, and PTB-ANQ 4CN CMP are summarized in Table S1.

## 3. Results and discussion

### 3.1. Characterization of the adsorbents [PTB-FO CMP, PTB-ANQ 2CN CMP, and PTB-ANQ 4CN CMP]

To examine the effect of cyano groups on dye adsorption, we synthesized three CMPs by polymerizing PTB with two bromine-containing monomers that have different numbers of cyano groups, along with a monomer lacking cyano groups.: FO-2Br, ANQ-2CN 2Br, and ANQ-4CN 2Br. The synthesis was conducted via the Sonogashira coupling reaction, yielding CMPs designated PTB-FO, PTB-ANQ 2CN, and PTB-ANQ 4CN CMPs, respectively. The complete synthetic procedures and reaction schemes are provided in Scheme 1. The chemical structures of the synthesized PTB-FO, PTB-ANQ 2CN, and PTB-ANQ 4CN CMPs were characterized using Fourier transform infrared (FT-IR) spectroscopy, solid-state $^{13}$C nuclear magnetic resonance (NMR) spectroscopy, and X-ray photoelectron spectroscopy (XPS). The FT-IR spectra of the PTB-FO, PTB-ANQ 2CN, and PTB-ANQ 4CN CMPs, shown in Fig. 1(a), exhibited key absorption bands at approximately 3048 $cm^{-1}$ and 1593 $cm^{-1}$ which were assigned to aromatic C-H and C═C stretching vibrations from benzene rings. In addition, both PTB-FO and PTB-ANQ 2CN CMPs had absorption bands at approximately 1716 and 1677 $cm^{-1}$, corresponding to the C═O groups in the FO and ANQ monomers. While the absorption bands at approximately 2192 $cm^{-1}$, correspond to the C≡C groups within the PTB structure and -C≡N- functional groups present in PTB-ANQ 2CN, and PTB-ANQ 4CN CMPs: respectively. An additional peak observed near 2191 $cm^{-1}$ was attributed to the C≡C groups within the PTB in the PTB-FO CMP. Raman spectroscopy confirmed the presence of CN groups, with characteristic peaks observed at approximately 2192 $cm^{-1}$ for both PTB-ANQ 2CN and PTB-ANQ 4CN CMPs [Figure S9]. The solid-state $^{13}$C NMR spectra, presented in Fig. 1(b), further confirmed the structural integrity of the three CMPs. Signals in the range of 70–90 ppm were attributed to symmetric C≡C units, whereas peaks in the 120–140 ppm range corresponded to carbon atoms in benzene rings. Additionally, a peak at approximately 118 ppm, positioned adjacent to the aromatic signals, confirmed the presence of C≡N moieties, which were

distinctly observed in the PTB-ANQ 2CN, and PTB-ANQ 4CN CMPs spectra. Carbon signals above 160 ppm were also observed for PTB-FO and PTB-ANQ 2CN CMPs, corresponding to C═O groups in their framework structures. Fig. 1(c) presents the XPS analysis results, revealing that the carbon (C) signals for PTB-FO, PTB-ANQ 2CN, and PTB-ANQ 4CN CMPs are consistently detected at 286 eV. Additionally, oxygen (O) signals are observed at 533 eV in PTB-FO and PTB-ANQ 2CN CMPs, while nitrogen (N) signals are detected at 401 eV in PTB-ANQ 2CN and PTB-ANQ 4CN CMPs. As illustrated in Figure S10(a), the C 1 s spectrum of PTB-FO CMP exhibited three distinct peaks at 284.7 eV, 287.2 eV, and 292.2 eV, corresponding to C═C/C– bonds, C═C bonds, and π–π interactions, respectively. Similarly, the C 1 s spectrum of PTB-ANQ 2CN CMP [Figure S10(b)] displayed three peaks at 284.7 eV, 286.4 eV, and 288.1 eV, which were assigned to C═C/C– bonds, –C≡N groups, and C═O bonds, respectively. In contrast, the C 1 s spectrum of PTB-ANQ 4CN CMP featured two peaks at 284.7 eV and 286.4 eV, attributed to C═C/C– bonds and –C≡N groups, respectively [Figure S10 (c)]. Thermogravimetric analysis (TGA) further elucidates the thermal stability of the synthesized CMPs [Fig. 1(d)]. The decomposition temperature at 5 % weight loss ($T_{d5}$) for PTB-FO, PTB-ANQ 2CN, and PTB-ANQ 4CN CMPs is determined to be 388.6 °C, 364.6 °C, and 342.1 °C, respectively, whereas their decomposition temperatures at 10 % weight loss ($T_{d10}$) are recorded as 442.9 °C, 471.7 °C, and 423.1 °C, respectively. Moreover, after heat treatment at 800 °C, the residual char yields of PTB-FO, PTB-ANQ 2CN, and PTB-ANQ 4CN CMPs are measured as

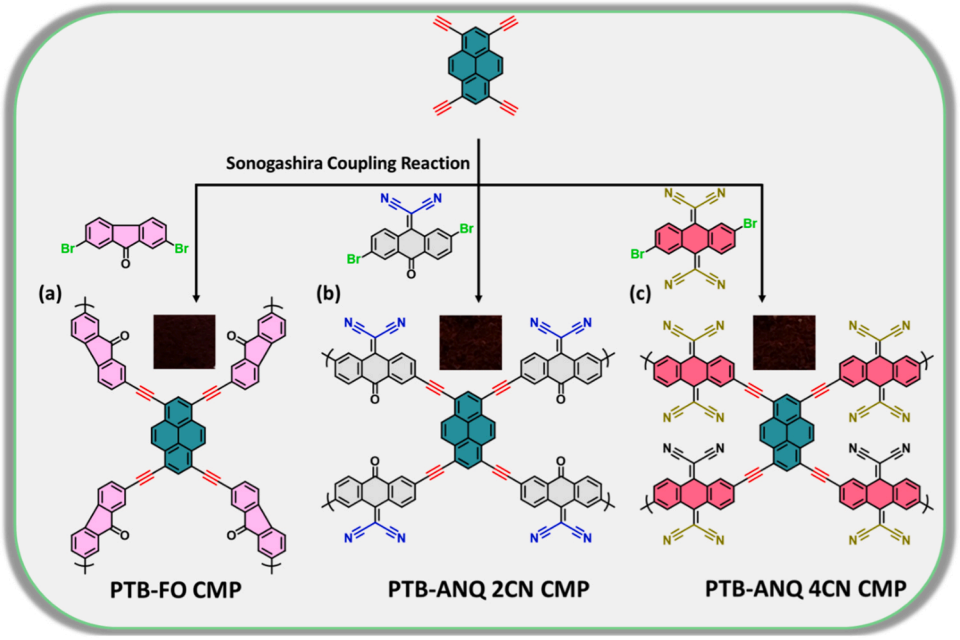


**Scheme 1.** Schematic scheme for the preparation of PTB-FO, PTB-ANQ-2CN and PTB-ANQ 4CN CMPs.

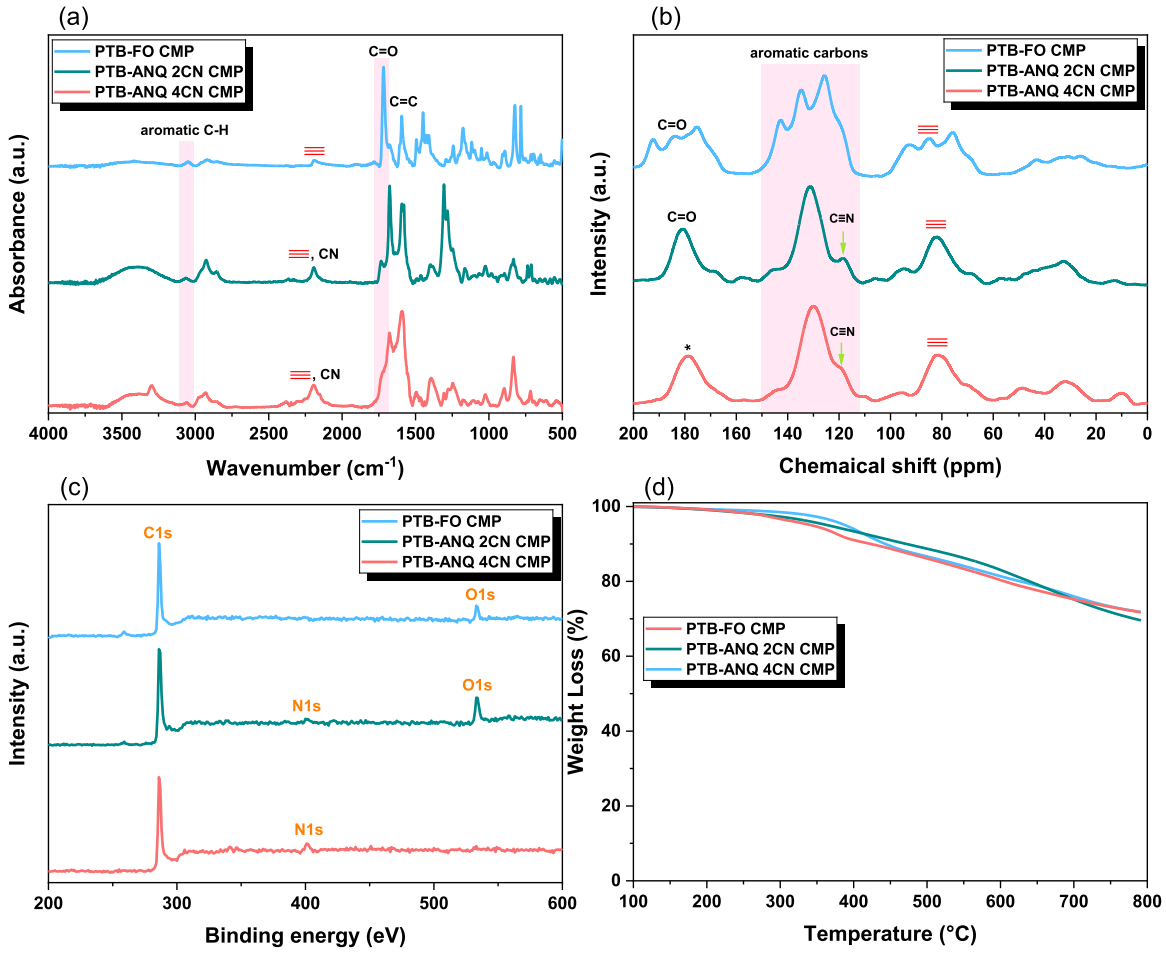


**Fig. 1.** (a) FTIR, (b) solid state $^{13}C$ NMR, (c) XPS, and (d) TGA analyses of the PTB-FO, PTB-ANQ-2CN and PTB-ANQ 4CN CMPs.

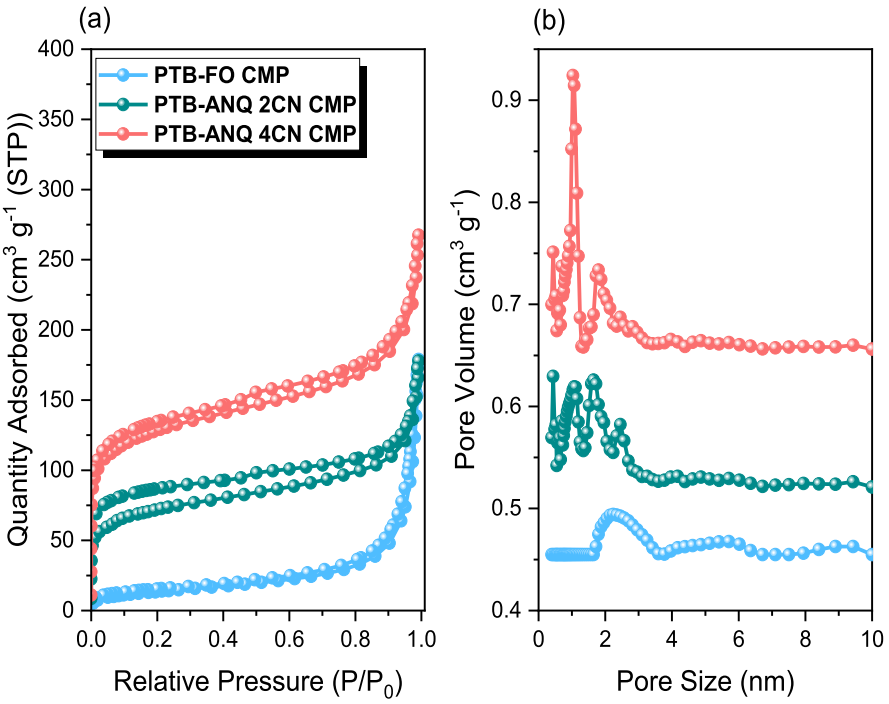


**Fig. 2.** (a) $N_2$ adsorption-desorption profiles and (b) pore size distribution of the PTB-FO, PTB-ANQ 2CN, and PTB-ANQ 4CN CMPs.

71.8 %, 69.5 %, and 71.7 %, respectively. The structural characteristics of the CMPs were further investigated through nitrogen adsorption-desorption isotherms, pore size distribution analysis, and Brunauer–Emmett–Teller (BET) surface area measurements [Figs. 2(a) and 2(b)]. According to the IUPAC classification, all three CMPs [PTB-FO, PTB-ANQ 2CN, and PTB-ANQ 4CN CMPs] exhibit type IV isotherms, indicative of mesoporous materials. The presence of $H_4$-type hysteresis loops in the isotherms suggests the existence of slit-shaped pores, which are typically associated with layered or plate-like structures [Fig. 2(a)]. BET analysis provides detailed insights into the textural properties of the synthesized CMPs. PTB-FO CMP exhibits a surface area of 51 $m^2/g$ and a pore volume of 0.2618 $cm^3/g$, with a predominant pore size centered around 2 nm, confirming its mesoporous nature with additional microporosity. In contrast, PTB-ANQ 2CN CMP demonstrates a significantly larger surface area of 236 $m^2/g$ and a pore volume of 0.257 $cm^3/g$,

with a broader pore size distribution ranging from 2 to 4 nm. Notably, PTB-ANQ 4CN CMP achieves the highest surface area of 465 $m^2/g$ and the largest pore volume of 0.4024 $cm^3/g$, with a dominant pore size range also spanning 2–4 nm [Fig. 2(b)]. These findings indicate a direct correlation between the cyano group content and the enhancement of surface area and pore volume, with the most pronounced improvement observed in PTB-ANQ 4CN CMP. The substantial increase in porosity and surface area in PTB-ANQ 4CN CMP aligns with its higher nitrogen adsorption capacity, underscoring the pivotal role of cyano functionalization in modifying the structural properties of the CMPs.

The scanning electron microscopy (SEM) images of PTB-FO, PTB-ANQ 2CN, and PTB-ANQ 4CN CMPs reveal distinct morphological characteristics for each material [Fig. 3]. As shown in Fig. 3(a-i), all three CMPs [PTB-FO, PTB-ANQ 2CN, and PTB-ANQ 4CN CMPs] exhibit irregularly shaped, aggregated particles of varying sizes, indicative of a disordered or amorphous structure. The absence of well-defined, sharp patterns in the images further confirms their non-crystalline nature, consistent with materials lacking long-range structural order. Comparative analysis indicates that PTB-ANQ 2CN and PTB-ANQ 4CN CMPs exhibit a more pronounced porous structure, characterized by a highly interconnected network of particles and well-defined pore spaces. The elemental SEM-EDS maps are shown in Figures S11-S13 illustrate the uniform distribution of C and O in the PTB-FO CMP, as well as the uniform distribution of C, O, and N in the PTB-ANQ 2CN and PTB-ANQ 4CN CMPs. This confirms the successful synthesis of these three CMPs via the Sonogashira coupling polymerization reaction. Transmission electron microscopy (TEM) further elucidates the structural features of these CMPs [PTB-FO, PTB-ANQ 2CN, and PTB-ANQ 4CN CMPs]. At higher magnifications, the TEM images confirm the presence of a porous and disordered framework in all three materials [Fig. 3(j-l) and Figure S14]. The irregular and non-uniform particle distribution observed in TEM analysis aligns with the amorphous nature identified in SEM, reinforcing the absence of long-range order within these CMP structures.

### *3.2. Adsorption studies of the adsorption of Rhodamine B on adsorbents [PTB-FO CMP, PTB-ANQ 2CN CMP, and PTB-ANQ 4CN CMP]*

#### *3.2.1. Effect of pH and contact time*

The pH of the solution plays a pivotal role in the adsorption behavior of RhB onto various adsorbents, as it directly influences both the ionization state of RhB molecules and the surface charge of the adsorbent. To systematically assess the impact of pH on the adsorption performance of the synthesized polymers, sorption experiments were conducted over a pH range of 1–7 at a constant temperature of 298 K. In these experiments, 5 mg of each CMP was introduced into an RhB solution with its pH precisely adjusted to the target value. The adsorption capacity was quantified after 24 h of equilibration to determine the extent of RhB removal under different pH conditions. This study provides critical insights into the pH-dependent adsorption mechanisms and the role of surface charge interactions in optimizing dye removal efficiency. As illustrated in Fig. 4(a), the adsorption efficiency of the synthesized CMPs was strongly influenced by the solution's pH, particularly before the introduction of cyano (CN) functional groups. In the case of PTB-FO CMP, the removal efficiency exhibited a pronounced increase with rising pH, starting at approximately 40 % at pH 1 and reaching nearly 100 % at pH 7, indicating enhanced adsorption under alkaline conditions. Upon the incorporation of two cyano groups, PTB-ANQ 2CN CMP demonstrated a significantly improved adsorption performance, with an initial removal efficiency of ~88 % at pH 1, which steadily increased to

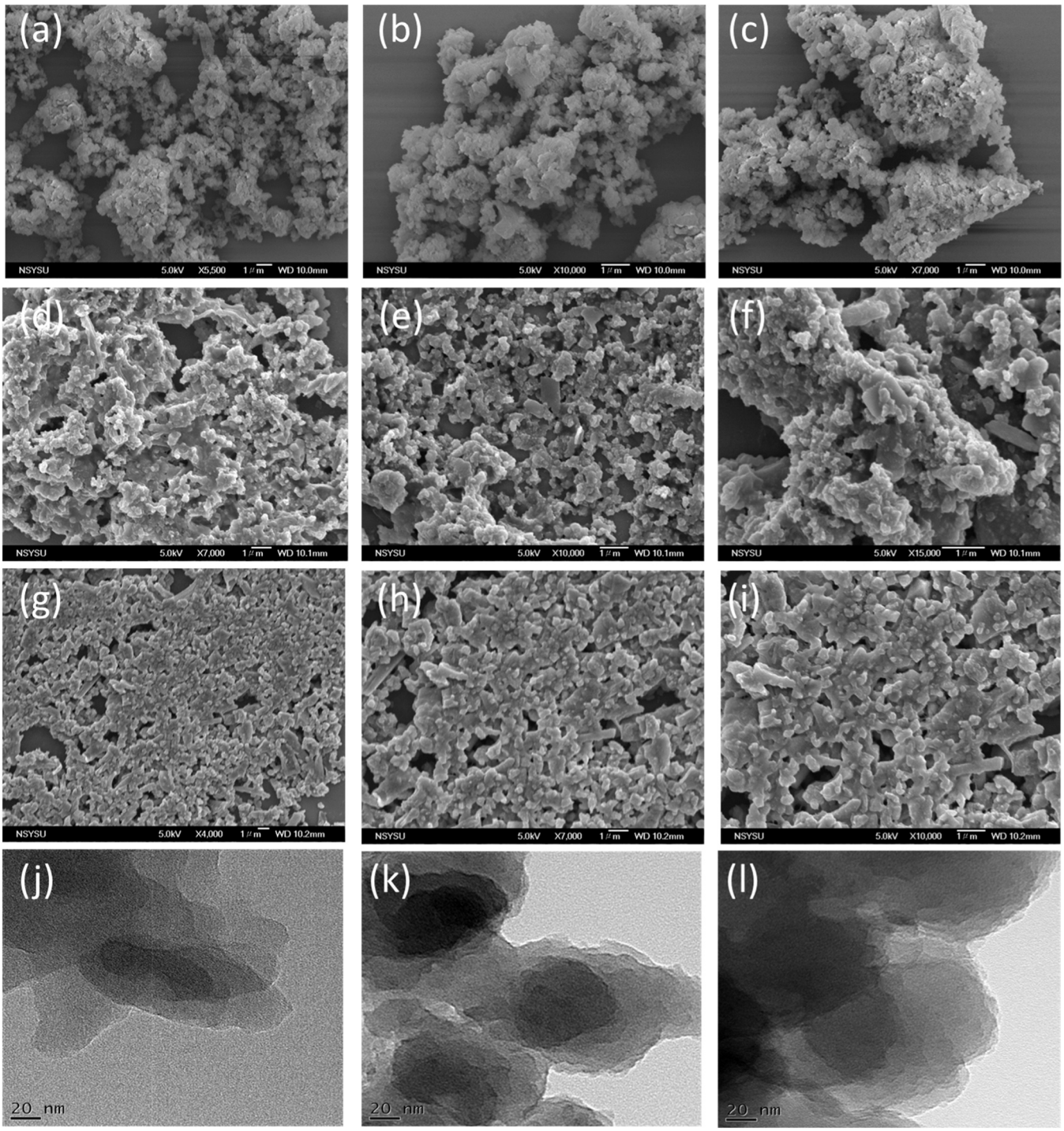


**Fig. 3.** (a-i) SEM images and (j-l) TEM images of the (a, b, c, j) PTB-FO, (d, e, f, k) PTB-ANQ 2CN, (g, h, i, l) PTB-ANQ 4CN CMPs.

nearly 100 % at pH 4 and above. This suggests that cyano groups enhance dye-polymer interactions, even under acidic conditions. For PTB-ANQ 4CN CMP, which contains a higher density of CN groups, the adsorption efficiency remained consistently high across the entire pH range, demonstrating minimal variation with pH fluctuations. This stability is likely attributed to the strong interaction between RhB and the abundant cyano functionalities, which maintain effective adsorption regardless of the solution's pH. Furthermore, the adsorption performance of PTB-ANQ 4CN CMP was unaffected by the protonation states of RhB, which transitions between $RhBH^{+}$, $RhBH_2^{2+}$, and the zwitterionic form (RhB±) depending on pH. The ability of PTB-ANQ 4CN CMP to sustain high adsorption efficiency across diverse pH conditions underscores its potential as a robust and versatile adsorbent for the removal of dyes from wastewater. Optimizing contact time is essential to ensure equilibrium in dye-adsorbent interactions, enabling a comprehensive evaluation of adsorption efficiency [81]. All three CMPs exhibited a rapid initial increase in RhB removal within the first 30 minutes [Fig. 4(b)], highlighting fast adsorption kinetics at the early stage. This behavior is typical of adsorption processes, where readily available active sites on the polymer facilitate rapid dye uptake. For PTB-FO CMP, the adsorption efficiency increased sharply at the beginning, followed by a gradual plateau as equilibrium was approached. The

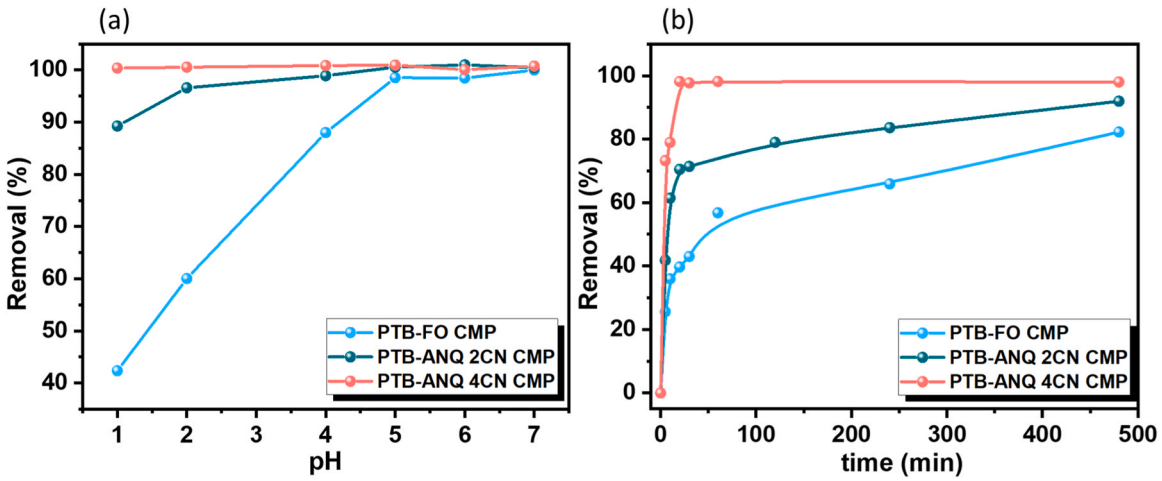


**Fig. 4.** (a) Effect of solution pH on adsorption of Rhodamine B on PTB-FO, PTB-ANQ 2CN and PTB-ANQ 4CN CMPs. (b) Effect of contact time on adsorption of Rhodamine B on PTB-FO, PTB-ANQ-2CN, and PTB-ANQ 4CN CMPs at pH 4.

removal efficiency stabilized at approximately 60 % after 120 minutes, indicating moderate adsorption capacity. Similarly, PTB-ANQ 2CN CMP demonstrated a rapid increase in RhB removal within the first 30 minutes, with adsorption continuing at a slower rate before reaching an equilibrium removal efficiency of ~90 % at 120 minutes. Among the three CMPs, PTB-ANQ 4CN CMP exhibited the highest and most rapid adsorption efficiency, achieving nearly 100 % RhB removal almost instantaneously and maintaining this efficiency throughout the remaining contact time. This suggests that the high density of cyano functional groups significantly enhances RhB adsorption, enabling a rapid and highly efficient equilibrium process.

### 3.3. Adsorption kinetics of RhB by PTB-FO CMP, PTB-ANQ 2CN CMP, and PTB-ANQ 4CN CMP

The kinetic analysis of RhB adsorption provides critical insights into the optimization of adsorption conditions for batch processes. Kinetic parameters, which describe the adsorption rate and mechanism, are essential for the development and design of efficient adsorption systems. Various kinetic models have been employed to evaluate adsorption behavior, enabling a deeper understanding of the adsorption dynamics. Non-linear regression analysis has emerged as a preferred approach for kinetic modeling, as it directly fits experimental data to the original kinetic equations, circumventing potential errors associated with linear transformations. This method enhances the accuracy of kinetic parameter estimation, ensuring a more reliable representation of adsorption behavior. The non-linear fittings of the experimental kinetic data to three commonly used adsorption models—pseudo-first-order, pseudo-second-order, and Elovich models [Equations S1-S3] are illustrated in Figures S15(a-c). The calculated kinetic parameters for RhB adsorption onto the synthesized PTB-FO CMP, PTB-ANQ 2CN CMP, and PTB-ANQ 4CN CMP are calculated according to the equations in Figure S15(d), and the data are summarized in Table S2. The data indicates that the pseudo-second-order model provides the best fit for the adsorption kinetics of PTB-ANQ 2CN CMP, and PTB-ANQ 4CN CMP suggests that the adsorption process is predominantly governed by chemisorption. This mechanism likely involves electron sharing or exchange interactions between the cyano-functionalized polymer surfaces and RhB dye molecules, facilitating strong and stable adsorption. Among the studied materials, PTB-ANQ 4CN CMP exhibits the highest initial adsorption rate, indicating that it possesses the most accessible active sites and exhibits the strongest interactions with RhB. In contrast, for Py-FO CMP, which lacks cyano functional groups, the Elovich model provides the best fit for the experimental data.

### 3.4. Adsorption isotherm study

To gain deeper insight into the surface characteristics and adsorption behavior of the adsorbents, the adsorption isotherm of RhB was investigated. In this study, 5 mg of each CMP was used to remove RhB from solutions with concentrations ranging from 10 ppm to 100 ppm. As illustrated in Fig. 5, PTB-FO CMP exhibited the lowest adsorption capacity, reaching approximately 40 mg/g, indicating that it saturates at lower concentrations compared to the other materials. PTB-ANQ 2CN CMP demonstrated a higher adsorption capacity of nearly 55 mg/g, though its adsorption rate increased more gradually than that of PTB-ANQ 4CN CMP. Among the tested materials, PTB-ANQ 4CN CMP exhibited the highest adsorption capacity, approaching 90 mg/g at higher concentrations. These findings suggest that increasing the number of CN groups enhances adsorption performance. Table S3 provides a detailed comparison of the RhB adsorption performance of our synthesized PTB-FO, PTB-ANQ 2CN, and PTB-ANQ 4CN CMP materials with previously reported adsorbents. The data highlights the adsorption capacities and efficiencies of our CMPs relative to other materials, demonstrating their potential advantages in dye removal applications.

### 3.5. Adsorption isotherm models

To assess the adsorption capacity of RhB dye onto three distinct CMPs and analyze the underlying mechanisms, the Langmuir,

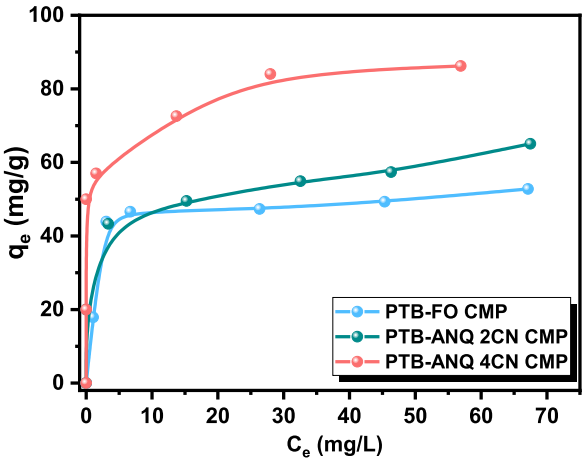


**Fig. 5.** Isotherm curve of RhB adsorption onto PTB-FO, PTB-ANQ 2CN, and PTB-ANQ 4CN CMPs.

Freundlich, and Temkin isotherm models were employed. Their non-linear forms are shown in Equations (S4) to (S6), with corresponding parameters summarized in Table S4. Figures S16(a-c) present the non-linear fit of the adsorption data for RhB onto PTB-FO, PTB-ANQ 2CN, and PTB-ANQ 4CN CMPs using various isotherm models. The accuracy of model fitting was assessed using correlation coefficients ($R^2$) and chi-square ($\chi^2$) tests, where a strong fit is indicated by higher $R^2$ and lower $\chi^2$ values (Table S4 and Figure S16(d)). The results demonstrate that the Langmuir model provided the best fit, as evidenced by the highest $R^2$ values (0.976, 0.993, and 0.999) and the lowest $\chi^2$ values (6.329, 1.291, and 0.008) for PTB-FO, PTB-ANQ 2CN, and PTB-ANQ 4CN CMPs, respectively. The strong agreement with the Langmuir model suggests a monolayer adsorption process, making it a suitable framework for differentiating between physical and chemical adsorption mechanisms. The adsorption mechanism of RhB onto various polymer adsorbents is influenced by multiple factors, including solution pH, the chemical structure of the adsorbent, and physicochemical interactions between RhB and the polymer surface. RhB exists in different protonation states depending on pH, which affects its adsorption behavior. At lower pH values, RhB predominantly exists in its protonated forms ($RhBH^+$ or $RhBH_2^{2+}$), enhancing electrostatic attraction with negatively charged adsorbent surfaces. As the pH increases, RhB transitions into a zwitterionic ($RhB^{\pm}$) or neutral form, reducing electrostatic interactions while favoring other mechanisms such as hydrogen bonding and van der Waals forces. The incorporation of CN groups in the CMPs framework significantly influences the adsorption mechanism. CN groups, being electron-withdrawing, modify the electron density of the polymer surface, promoting enhanced interactions through hydrogen bonding, dipole-dipole interactions, and π-π stacking with the aromatic rings of RhB. Furthermore, the presence of CN groups may contribute to adsorption stability across a wide pH range. This is evident in the case of PTB-ANQ 4CN CMPs, where adsorption capacity remained consistent despite pH variations, indicating a robust and versatile adsorption mechanism.

### 3.6. Adsorption thermodynamics

The adsorption behavior of RhB onto the three materials—PTB-FO CMP, PTB-ANQ 2CN CMP, and PTB-ANQ 4CN CMP—was investigated across a range of temperatures (30–80 °C) [Fig. 6(a-c)]. Temperature can directly impact the adsorption process due to the effects of Brownian motion. Notably, all three CMP adsorption capacities increased significantly as the temperature was elevated from 30 to 80 °C. The thermodynamic parameters—Gibbs free energy change (ΔG), enthalpy change (ΔH), and entropy change (ΔS)—are essential for understanding how temperature influences dye absorption. Eqs. (1)–(3) describe the interrelation among these parameters.

$$K_d = \frac{q_e}{C_e} \tag{1}$$

$$\ln K_d = -\frac{\Delta H}{RT} + \frac{\Delta S}{R} \tag{2}$$

$$\Delta G = -RT\ln K_d \tag{3}$$

In these expressions, $q_e$ denotes the equilibrium adsorption capacity of RhB (mg $g^{-1}$), $C_e$ represents the equilibrium concentration of the dye in solution (mg $L^{-1}$), and $K_d$ refers to the Langmuir adsorption constant (L $g^{-1}$). R is the universal gas constant (0.008314 KJ $mol^{-1}$ $K^{-1}$), and T is the absolute temperature in Kelvin. The values of ΔH and ΔS were

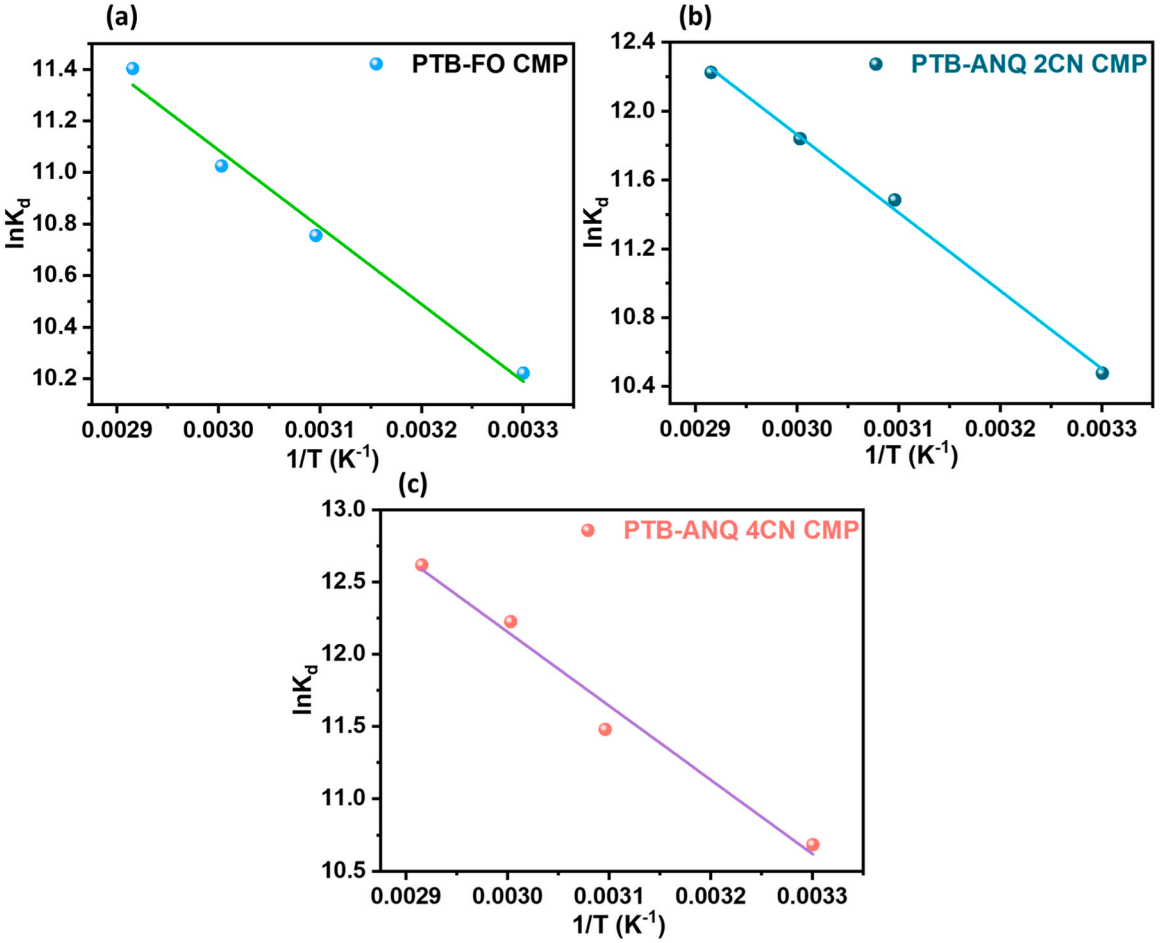


**Fig. 6.** Plot of $\ln K_d$ versus 1/T for adsorption of RhB onto (a) PTB-FO CMP, (b) PTB-ANQ 2CN CMP, and (c) PTB-ANQ 4CN CMP.

**Table 1**
Thermodynamic parameters for adsorption of rhodamine B onto PTB-FO CMP, PTB-ANQ 2CN CMP, and PTB-ANQ 4CN CMP.

| CMP | Parameters | | | |
|---|---|---|---|---|
| | Temperature | $G^0$ (kJ/mol) | $H^0$ (kJ/mol) | $S^0$ (J/mol.K) |
| PTB-FO | 303 | −25.750 | 24.839 | 0.166 |
| | 323 | −28.883 | | |
| | 333 | −30.525 | | |
| | 343 | −32.517 | | |
| PTB-ANQ 2CN | 303 | −26.392 | 37.710 | 0.212 |
| | 323 | −30.839 | | |
| | 333 | −32.777 | | |
| | 343 | −34.861 | | |
| PTB-ANQ 4CN | 303 | −26.914 | 42.558 | 0.229 |
| | 323 | −30.829 | | |
| | 333 | −33.849 | | |
| | 343 | −35.983 | | |

calculated from the slope and intercept of the linear plot of ln $K_d$ against 1/T. The thermodynamic data are summarized in Table 1. Notably, the negative values of ΔG became more pronounced with increasing temperature, indicating that the adsorption process is spontaneous and becomes more favorable as the temperature rises. These results indicate that the adsorption process is more favorable at higher temperatures. The positive ΔH value confirms that the adsorption of RhB onto the adsorbent is endothermic. Furthermore, the positive ΔS value suggests randomness at the solid–liquid interface during adsorption. Overall, the thermodynamic parameters (ΔG, ΔH, and ΔS) support the conclusion that the three CMPs are an effective and promising adsorbent for the removal of RhB from wastewater.

The PTB-FO, PTB-ANQ 2CN, and PTB-ANQ 4CN CMPs incorporate polar functional groups, including carbonyl (C═O) and cyano (CN) moieties, which play a pivotal role in governing dye adsorption behavior. Adsorption efficiency is largely dictated by the chemical functionalities present on the adsorbent surface and the structural features of the dye. RhB, a cationic dye bearing one carboxylic acid and two amino groups, exhibits strong affinity toward the CMP networks due to electrostatic interactions. Moreover, the planar aromatic structure of RhB facilitates π–π stacking with the conjugated backbones of the CMPs, further promoting adsorption, as evidenced in Figure S17.

### 3.7. DFT study

We conducted DFT calculations on all building units [PTB, FO-2Br, ANQ-2CN 2Br, ANQ-4CN 2Br], CMPs [PTB-FO, PTB-ANQ 2CN, and PTB-ANQ 4CN CMPs], and RhB to determine their geometrical structures and electronic properties. The HOMO and LUMO energy levels of these molecules were calculated at the B3LYP-D3(BJ)/6–31 G(d) level. Figure S18 presents the HOMO-LUMO isosurface maps of PTB, FO-2Br, ANQ-2CN 2Br, ANQ-4CN 2Br, and RhB, providing valuable insight into their electronic and orbital distributions. Our calculations reveal that these molecules exhibit high conjugation, with both HOMO and LUMO delocalized across the entire conjugated system. Among them, PTB has the smallest HOMO-LUMO energy gap (2.97 eV), while FO-2Br, ANQ-2CN 2Br, and ANQ-4CN 2Br have gaps of 3.9, 3.75, and 3.44 eV; respectively. In the case of RhB, the HOMO is primarily composed of the lone pairs on the Cl atom, whereas the LUMO is distributed over the xanthene ring. Upon polymerization, we observe a substantial reduction in the HOMO-LUMO gap, as depicted in Fig. 7. This narrowing enhances the reactivity of the resulting polymers. Among them, PTB-ANQ 4CN CMP exhibits the highest reactivity, with a significantly low HOMO-LUMO gap of 1.75 eV. PTB-FO and PTB-ANQ 2CN CMP have slightly higher gaps of 2.32 and 2.03 eV, respectively. This reduction compared to the individual building units is attributed to the extended conjugation in the polymerized structures. Furthermore, the HOMO and LUMO distributions in the CMPs show distinct localization patterns: the HOMO is predominantly localized on the pyrene moiety, while the LUMO is extended over the side arms. The pyrene moiety remains highly planar, facilitating strong conjugation throughout the CMP backbone. Figure S19 presents the molecular electrostatic potential (MESP) analysis of the PTB, FO-2Br, ANQ-2CN 2Br, and ANQ-4CN 2Br, providing a quantitative representation of electrophilic and nucleophilic sites. This analysis highlights the most reactive regions within each molecule. Areas with high electron density, indicating strong negative potential,

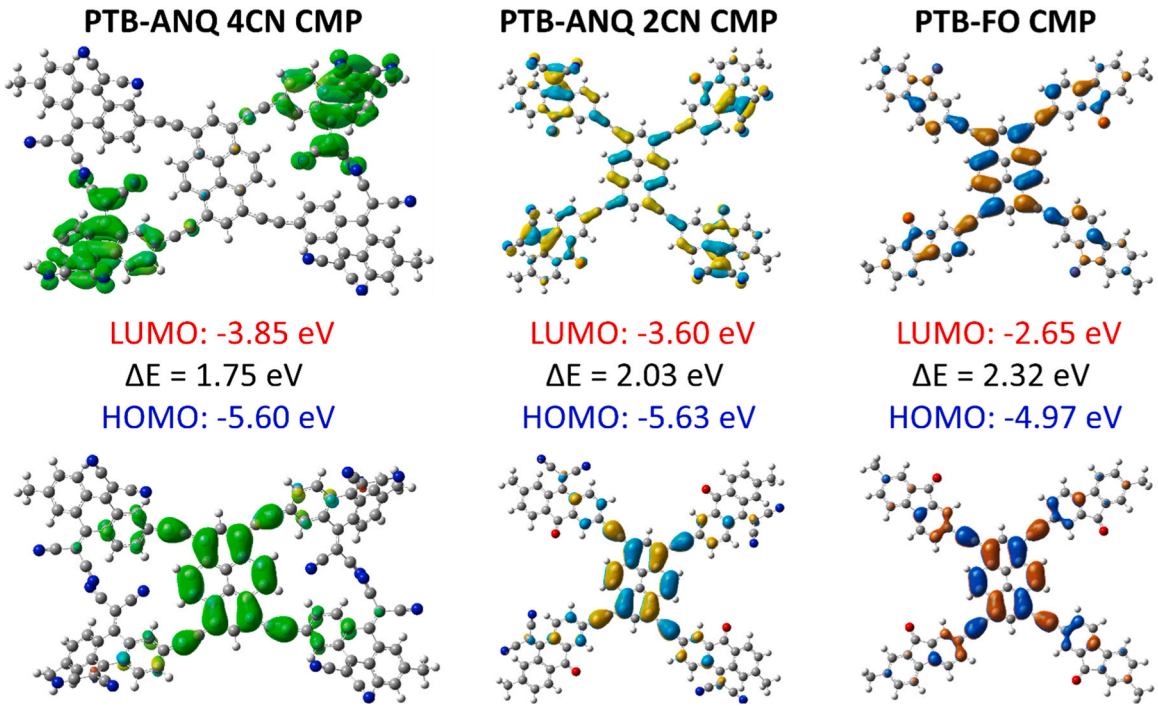


**Fig. 7.** The HOMO and LUMO isosurface maps of the PTB-ANQ 4CN CMP, PTB-ANQ 2CN CMP, and PTB-FO CMP along with their energies calculated at the B3LYP-D3(BJ)/6–31 G(d) level.

are shown in red, while areas with low electron density, representing positive potential, are depicted in blue. In PTB, the highest electron density (intense red regions) is concentrated around the triple bonds, corresponding to the areas of the highest negative potential. Conversely, the terminal hydrogen atoms of the acetylene arms exhibit the highest positive potential. For FO-2Br, ANQ-2CN 2Br, and ANQ-4CN 2Br, the cyano and carbonyl groups are the primary sites of high negative potential. Notably, the carbonyl group in FO-2Br has the highest negative potential, measured at −36 kcal/mol, making it the most nucleophilic site among the four molecules. This strong nucleophilicity arises due to the unidirectional electron-withdrawing effect of the functional groups

Figure S20 illustrates the MESP maps of the PTB-FO, PTB-ANQ 2CN, and PTB-ANQ 4CN CMPs alongside RhB, highlighting their electrophilic and nucleophilic regions. Among the polymers, the most nucleophilic site is the carbonyl group in PTB-FO CMP, which exhibits a negative potential of −35 kcal/mol. In PTB-ANQ 2CN and PTB-ANQ 4CN CMPs, the cyano groups also display significant nucleophilicity, with an electrostatic potential of −33 kcal/mol. The most electrophilic regions are found at the terminal hydrogen atoms of the side arms, indicating areas of low electron density. In the case of RhB, the highest electron density is concentrated around the Cl anion and its surrounding area, making it the most nucleophilic region within the molecule. Table S5 presents the calculated global reactivity descriptors for all molecules, obtained using DFT at the same level of theory [82]. The energy of the HOMO ($E_{HOMO}$) and LUMO ($E_{LUMO}$) provides insight into the molecule's electron-donating and electron-accepting tendencies, respectively. The HOMO-LUMO energy gap, which represents the energy difference between these orbitals, serves as an indicator of molecular reactivity: a smaller gap corresponds to higher reactivity. Among the first four molecules listed in Table S5, PTB exhibits the highest $E_{HOMO}$ (lowest ionization potential, IP), making it the most efficient electron donor. Conversely, ANQ-4CN 2Br has the lowest $E_{LUMO}$ (highest electron affinity, EA), indicating its strong electron-accepting ability due to the electron-withdrawing nature of the cyano groups. Additionally, ANQ-4CN 2Br possesses the highest electronegativity ($\chi$) and electrophilicity index ($\omega$), as well as the greatest capacity to accept electrons (highest $\Delta N_{max}$). These findings suggest that upon polymerization, electron transfer occurs from PTB to the other three molecules. The fraction of electron transfer ($\Delta N$) from PTB to these acceptor molecules can be quantitatively estimated using Pearson's theory, as expressed by the equation [83]:

$$\Delta N = (\chi_{\text{molecule}} - \chi_{\text{Py}})/2(\eta_{\text{molecule}} + \eta_{\text{Py}})$$

The calculated fraction of electron transfer ($\Delta N$) for ANQ-4CN 2Br, ANQ-2CN 2Br, and FO-2Br is 0.24, 0.19, and 0.03, respectively. Among the three polymers, PTB-FO CMP is identified as the best electron donor due to its highest $E_{HOMO}$, whereas PTB-ANQ 4CN CMP serves as the most efficient electron acceptor, as expected. The highest reactivity is observed in PTB-ANQ 4CN CMP, followed by PTB-ANQ 2CN CMP. CMPs containing cyano groups exhibit higher electronegativity, with PTB-ANQ 4CN CMP (which has four cyano groups) being the most electronegative, followed by PTB-ANQ 2CN CMP (which has two cyano groups). Additionally, PTB-ANQ 4CN CMP possesses the highest electrophilicity index and $\Delta N_{max}$, reinforcing its strong electron-accepting ability. Compared to the three CMPs, the dye demonstrates superior electron-donating ability and lower electronegativity, suggesting that electron transfer will occur from the dye to the CMP upon adsorption. The calculated $\Delta N$ values for electron transfer from the dye to PTB-ANQ 4CN CMP, PTB-ANQ 2CN CMP, and PTB-FO CMP are 0.31, 0.26, and 0.05, respectively. Notably, PTB-ANQ 4CN CMP and PTB-ANQ 2CN CMP exhibit significantly stronger interactions with the dye than PTB-FO CMP. This can be attributed to the electron-withdrawing effect of the cyano groups, which enhances the CMPs' ability to accept electrons from the dye, thereby strengthening their interaction. As a result, PTB-ANQ 4CN CMP and PTB-ANQ 2CN CMP are expected to demonstrate superior performance in dye removal compared to PTB-FO CMP. Moreover, all CMPs exhibit stronger interactions (higher $\Delta N$ and $\Delta N_{max}$) than their respective building units, further emphasizing the enhanced electronic properties induced by polymerization. DFT is one of the most widely used techniques for investigating dye removal mechanisms from water. In this study, we employed DFT calculations to determine the adsorption energy and geometry of RhB on all three polymers. Fig. 8**(a)** presents the reduced density gradient (RDG) plots of RhB adsorbed on the CMPs surfaces. RDG plots are powerful tools for visualizing non-covalent interactions within and between molecules. As shown in Fig. 8 **(a)**, the interaction between the CMPs and the dye is primarily governed by van der Waals forces, represented by the green surface. Figure S21 presents the geometries of the dye–CMP complexes, where in both the PTB-ANQ 4CN CMP and PTB-ANQ 2CN CMP, the CMP arms enclose the dye molecule, promoting extensive interactions and resulting in enhanced adsorption energies. Additionally, π-π stacking interactions are observed between the pyrene moiety of the CMPs and the xanthene ring of the dye, further stabilizing the adsorption. The calculated adsorption energies ($E_{ads}$) of RhB on PTB-ANQ 4CN CMP, PTB-ANQ 2CN CMP, and PTB-FO CMP are −60.5, −58.4, and −40.5 kcal/mol, respectively. These high adsorption energy values confirm the strong stability of the dye-polymer complexes, reinforcing the effectiveness of the three CMPs in capturing and removing RhB from water. The removal efficiency follows the order PTB-ANQ 4CN CMP > PTB-ANQ 2CN CMP > PTB-FO CMP, which aligns with our previous computational findings and is expected to be supported by experimental results. To better understand the effect of binding on the geometry of both the dye and the polymers, Fig. 8(b) presents their optimized structures along with selected geometrical parameters before and after adsorption. RhB exhibits a flexible molecular structure, allowing free rotation around several single bonds. Upon adsorption, the dye undergoes significant conformational changes, with several torsional angles twisting to maximize its interaction with the CMPs. A similar structural adaptation is observed in all three CMPs, where the four side arms adjust their orientations to accommodate the dye, thereby enhancing the overall interaction.

## 4. Conclusions

This study focuses on the design and development of cyano-functionalized CMPs to enhance dye adsorption efficiency. Three CMPs—PTB-FO, PTB-ANQ 2CN, and PTB-ANQ 4CN CMPs were synthesized with varying cyano group content to investigate their adsorption performance for RhB. Experimental results revealed that the presence of cyano groups significantly improved dye removal efficiency, with PTB-ANQ 4CN CMP exhibiting the highest adsorption capacity due to its strong and stable interactions with RhB molecules. Adsorption behavior was analyzed using kinetic and isotherm models. Kinetic studies confirmed that the pseudo-second-order model best described the adsorption process, indicating chemisorption as the dominant mechanism. The Langmuir isotherm model provided the best fit to the data, suggesting a monolayer adsorption mechanism on the polymer surface. The maximum adsorption capacity of PTB-ANQ 4CN CMP for RhB was determined to be 90 mg/g, highlighting its superior performance. Theoretical calculations show that RhB exhibits strong adsorption on PTB-ANQ 4CN CMP (−60.5 kcal/mol), PTB-ANQ 2CN CMP (−58.4 kcal/mol), and PTB-FO CMP (−40.5 kcal/mol), indicating stable dye–polymer interactions and the formation of robust dye–polymer complexes. Overall, this research demonstrates the potential of cyano-functionalized CMPs as effective adsorbents for environmental remediation. Their high adsorption capacity and stability offer a promising and sustainable approach to removing hazardous dyes from wastewater.

## CRediT authorship contribution statement

**Nian-Ping Chen:** Formal analysis, Data curation, Conceptualization. **Ahmed A. K. Mohammed:** Formal analysis. **Mohamed Gamal Mohamed:** Writing – review & editing, Writing – original draft,

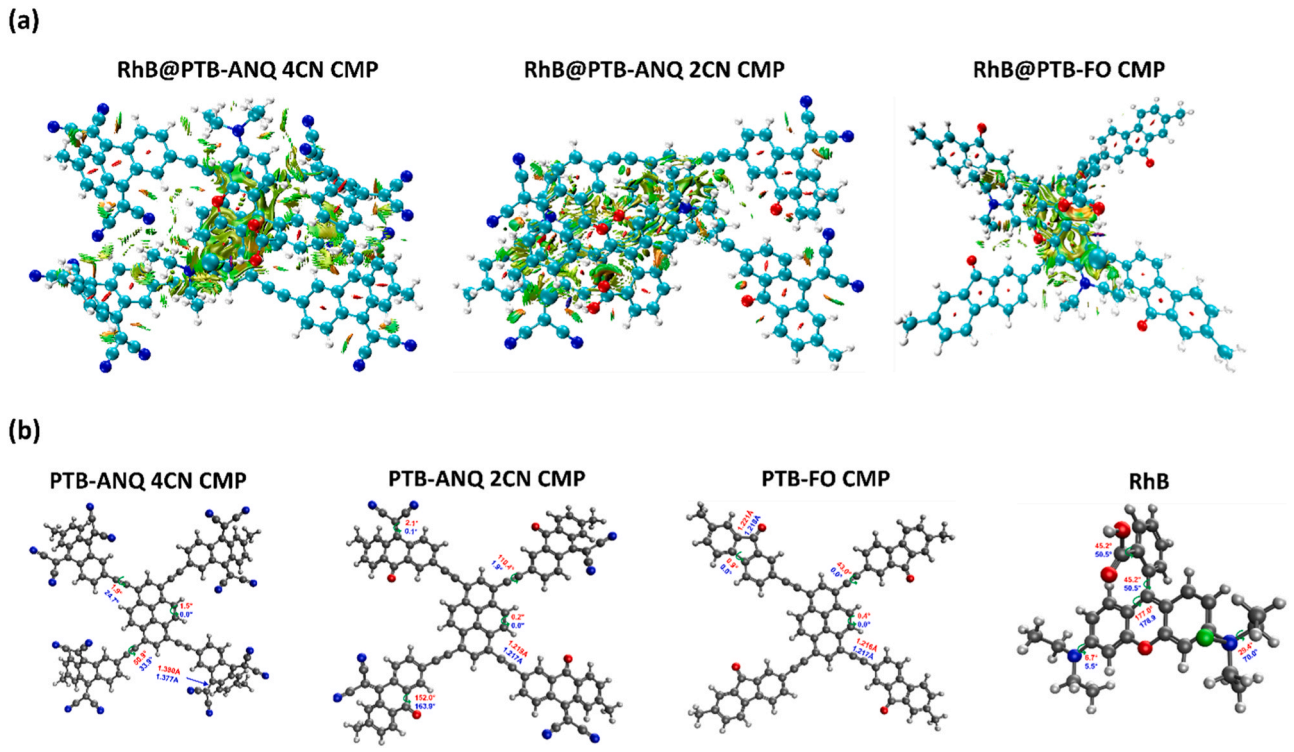


**Fig. 8.** (a) The geometry and intermolecular interactions for the RhB dye adsorbed on the surface of PTB-ANQ 4CN CMP, PTB-ANQ 2CN CMP, and PTB-FO CMP obtained by the Multiwfn program[F] on geometries optimized at the B3LYP-D3(BJ)/6–31 G(d) level. Color: The green surface between the two molecules indicates van der Waals interactions. (b) The structure and key geometrical parameters of PTB-ANQ 4CN CMP, PTB-ANQ 2CN CMP, PTB-FO CMP, and RhB were optimized at the B3LYP-D3(BJ)/6–31 G(d) level before and after adsorption. Parameters before adsorption are in blue and after adsorption in red color.

Supervision, Methodology, Investigation, Formal analysis, Data curation, Conceptualization. **Ahmed M. Elewa:** Writing – original draft, Supervision, Data curation, Conceptualization. **Shiao-Wei Kuo:** Supervision, Resources, Project administration.

## Declaration of Competing Interest

The authors declare that they have no known competing financial interests or personal relationships that could have appeared to influence the work reported in this paper.

## Acknowledgements

This study was supported financially by the National Science and Technology Council, Taiwan, under contracts NSTC 113-2223-E-110-001- and 113-2221-E-110–012-MY3. The authors thank the staff at National Sun Yat-sen University for their assistance with the TEM (ID: EM022600) experiments.

## Appendix A. Supporting information

Supplementary data associated with this article can be found in the online version at doi:10.1016/j.colsurfa.2025.137214.

## Data availability

The data that has been used is confidential. Data will be made available on request.

## References

[1] Y. Han, W. Li, J. Zhang, H. Meng, Y. Xu, X. Zhang, Adsorption behavior of Rhodamine B on nanoporous polymers, RSC Adv. 5 (2015) 104915–104922, https://doi.org/10.1039/C5RA21130A.

[2] H. Sadegh, G.A.M. Ali, V.K. Gupta, A.S.H. Makhlouf, R. Shahryari-ghoshekandi, M. N. Nadagouda, M. Sillanpää, E. Megiel, The role of nanomaterials as effective adsorbents and their applications in wastewater treatment, J. Nanostruct. Chem. 7 (2017) 1–14, https://doi.org/10.1007/s40097-017-0219-4.

[3] M. Afshari, M. Dinari, Synthesis of new imine-linked covalent organic framework as high efficient absorbent and monitoring the removal of direct fast scarlet 4BS textile dye based on mobile phone colorimetric platform, J. Hazard. Mater. 385 (2020) 121514, https://doi.org/10.1016/j.jhazmat.2019.121514.

[4] R. Bera, M. Ansari, S. Mondal, N. Das, Selective $CO_2$ capture and versatile dye adsorption using a microporous polymer with triptycene and 1,2,3-triazole motifs, Eur. Polym. J. 99 (2018) 259–267, https://doi.org/10.1016/j.eurpolymj.2017.12.029.

[5] B. Wang, Y. Liao, T. Wang, Metal oxide particle electrodes for degradation of high concentration phenol wastewater via electrocatalytic advanced oxidation, Chin. J. Chem. Eng. 75 (2024) 204–213, https://doi.org/10.1016/j.cjche.2024.09.006.

[6] S. Liu, Y. Guo, S. Yi, S. Yan, C. Ouyang, F. Deng, C. Li, G. Liao, Q. Li, Facile synthesis of pure silicon zeolite-confined silver nanoparticles and their catalytic activity for the reduction of 4-nitrophenol and methylene blue, Sep. Purif. Technol. 307 (2023) 122727, https://doi.org/10.1016/j.seppur.2022.122727.

[7] S. Liu, F. Deng, Y. Guo, C. Ouyang, S. Yi, C. Li, G. Liao, Q. Li, Silver nanocatalysts supported by multiple melanin carriers with a photothermal effect for reduction of methylene blue and 4-nitrophenol, ACS Appl. Nano Mater. 7 (2024) 889–903, https://doi.org/10.1021/acsanm.3c04882.

[8] I. Ali, New generation adsorbents for water treatment, Chem. Rev. 122 (2012) 5073–5091, https://doi.org/10.1021/cr300133d.

[9] J. Tang, R. Xu, G. Sui, D. Guo, Z. Zhao, S. Fu, X. Yang, Y. Li, J. Li, Double-shelled porous g-$C_3N_4$ nanotubes modified with amorphous Cu-Doped FeOOH nanoclusters as 0D/3D non-homogeneous photo-Fenton catalysts for effective removal of organic dyes, Small 19 (2023) 202208232, https://doi.org/10.1002/smll.202208232.

[10] W. Gong, Q. Wu, L. Ma, W. Zhang, X. Li, A. Xu, S. Zhao, $MnO_x$/g-$C_3N_4$ nanocomposites mediated sulfite activation for enhanced organic pollutants degradation under visible light irradiation, Colloids Surf. A Physicochem. Eng. Asp. 659 (2022) 130598, https://doi.org/10.1016/j.colsurfa.2022.130812.

[11] J. Núñez, M. Yeber, N. Cisternas, R. Thibaut, P. Medina, C. Carrasco, Application of electrocoagulation for the efficient pollutants removal to reuse the treated wastewater in the dyeing process of the textile industry, J. Hazard. Mater. 371 (2019) 705–711, https://doi.org/10.1016/j.jhazmat.2019.03.030.

[12] D. Lan, H. Zhu, J. Zhang, S. Li, Q. Chen, C. Wang, T. Wu, M. Xu, Adsorptive removal of organic dyes via porous materials for wastewater treatment in recent decades: a review on species, mechanisms and perspectives, Chemosphere 293 (2022) 133464, https://doi.org/10.1016/j.chemosphere.2021.133464.

[13] S. Afroze, T.K. Sen, A review on heavy metal ions and dye adsorption from water by agricultural solid waste adsorbents, Water Air Soil Pollut. 229 (2018) 1–50, https://doi.org/10.1007/s11270-018-3869-z.
[14] Saruchi, V. Kumar, Adsorption kinetics and isotherms for the removal of rhodamine B dye and $Pb^{+2}$ ions from aqueous solutions by a hybrid ion-exchanger, Arab. J. Chem. 12 (2019) 316–329, https://doi.org/10.1016/j.arabjc.2016.11.009.
[15] C.-W. Hsiao, A.M. Elewa, M.G. Mohamed, M.G. Kotp, M.M.-C. Chou, S.-W. Kuo, Designing strategically functionalized hybrid porous polymers with octavinylsilsesquioxane/dibenzo[g,p]chrysene/benzo[c]-1,2,5-thiadiazole units for rapid removal of Rhodamine B dye from water, Colloids Surf. A Physicochem. Eng. Asp. 699 (2024) 134658, https://doi.org/10.1016/j.colsurfa.2024.134658.
[16] A.A. Al-Gheethi, Q.M. Azhar, P. Senthil Kumar, A.A. Yusuf, A.K. Al-Buriahi, R.M. S. Radin Mohamed, M.M. Al-Shaibani, Sustainable approaches for removing Rhodamine B dye using agricultural waste adsorbents: a review, Chemosphere 287 (2022) 132080, https://doi.org/10.1016/j.chemosphere.2021.132080.
[17] L. Jin, Y.L. Li, J. Zhou, C.M. Huang, X. Liu, Rhodamine B as an efficient multifunctional passivator for the improvement of perovskite solar cell performance, J. Mater. Chem. C 11 (2023) 9189–9200, https://doi.org/10.1039/D3TC00818E.
[18] M.A. Arasi, A. Salem, S. Salem, Extraction of nano-porous silica from hydrosodalite produced via modification of low-grade kaolin for removal of methylene blue from wastewater, J. Chem. Technol. Biotechnol. 95 (2020) 1989–2000, https://doi.org/10.1002/jctb.6387.
[19] Z. Chai, B. Liu, P. Lv, Y. Bai, J. Wang, X. Song, W. Su, G. Yu, Recycling of coal gasification fine slag as ultra-high capacity adsorbents for the removal of Rhodamine B dye: graded synthesis method, kinetics and adsorption mechanism, Fuel 333 (2023) 126318, https://doi.org/10.1016/j.fuel.2022.126318.
[20] U. Jinendra, D. Bilehal, B.M. Nagabhushana, A.P. Kumar, Adsorptive removal of Rhodamine B dye from aqueous solution by using graphene–based nickel nanocomposite, Heliyon 7 (2021) e06851, https://doi.org/10.1016/j.heliyon.2021.e06851.
[21] C.-W. Hsiao, A.M. Elewa, M.G. Mohamed, S.-W. Kuo, Highly stable hybrid porous polymers containing polyhedral oligomeric silsesquioxane (POSS)/Dibenzo[g,p] chrysene and Dibenzo[b,d]thiophene units for efficient Rhodamine B dye removal, Sep. Purif. Technol. 332 (2024) 125771, https://doi.org/10.1016/j.seppur.2023.125771.
[22] W.S. Koe, J.W. Lee, W.C. Chong, Y.L. Pang, L.C. Sim, An overview of photocatalytic degradation: photocatalysts, mechanisms, and development of photocatalytic membrane, Environ. Sci. Pollut. Res. 27 (2020) 2522–2565, https://doi.org/10.1007/s11356-019-07193-5.
[23] T. Guo, X. Fan, X. Jiang, Y. Qi, J. Du, A. Zhang, H. Wang, Engineering shape of BiOCl nanosheets with improved visible-light response for superior photocatalytic degradation of Rhodamine B, J. Alloy. Compd. 948 (2023) 169586, https://doi.org/10.1016/j.jallcom.2023.169586.
[24] A.K. Behera, K.P. Shadangi, P.K. Sarangi, Efficient removal of Rhodamine B dye using biochar as an adsorbent: Study the performance, kinetics, thermodynamics, adsorption isotherms and its reusability, Chemosphere 354 (2024) 141702, https://doi.org/10.1016/j.chemosphere.2024.141702.
[25] Md Ahmaruzzaman, S.R. Mishra, Photocatalytic performance of g-$C_3N_4$ based nanocomposites for effective degradation/removal of dyes from water and wastewater, Mater. Res. Bull. 143 (2021) 111417, https://doi.org/10.1016/j.materresbull.2021.111417.
[26] X. Chen, H. Li, W. Liu, X. Zhang, Z. Wu, S. Bi, W. Zhang, H. Zhan, Effective removal of methyl orange and rhodamine B from aqueous solution using furfural industrial processing waste: Furfural residue as an eco-friendly biosorbent, Colloids Surf. A Physicochem. Eng. Asp. 583 (2019) 123976, https://doi.org/10.1016/j.colsurfa.2019.123976.
[27] F. Amalina, A.S.A. Razak, S. Krishnan, A.W. Zularisam, M. Nasrullah, A review of eco-sustainable techniques for the removal of Rhodamine B dye utilizing biomass residue adsorbents, Phys. Chem. Earth (Pt AB,C. ). 128 (2022) 103267, https://doi.org/10.1016/j.pce.2022.103267.
[28] M.R. Mahmoud, G.M. Rashad, E. Metwally, E.A. Saad, A.M. Elewa, Adsorptive removal of $^{134}Cs^{+}$, $^{60}Co^{2+}$ and $^{152+154}Eu^{3+}$ radionuclides from aqueous solutions using sepiolite: single and multi-component systems, Appl. Clay Sci. 141 (2017) 72–80, https://doi.org/10.1016/j.clay.2016.12.021.
[29] B. Isik, Adsorptive removal of hazardous rhodamine B dye from aqueous solutions by St. John's wort (Hypericum perforatum), Biomass-.-. Conv. Bioref. 15 (2024) 9553–9564, https://doi.org/10.1007/s13399-024-05840-7.
[30] M.S. Akhtar, S. Ali, W. Zaman, Innovative adsorbents for pollutant removal: exploring the latest research and applications, Molecules 29 (2024) 4317, https://doi.org/10.3390/molecules29184317.
[31] X.-C. Du, J.-H. Zhu, Z.-J. Quan, X.-C. Wang, Adsorption of rhodamine B by organic porous materials rich in nitrogen, oxygen, and sulfur heteroatoms, N. J. Chem. 45 (2021) 3448–3453, https://doi.org/10.1039/D0NJ05750A.
[32] A. Rajabizadeh, H. Abdipour, H.J. Mansoorian, A new approach for the elimination of Rhodamine B dye using a combination of activated persulfate and dithionite in the presence of magnetic fields, Chem. Eng. Process. Process. Intensif. 209 (2025) 110160, https://doi.org/10.1016/j.cep.2025.110160.
[33] N. Sheraza, A. Shah, A. Haleem, F.J. Iftikhar, Comprehensive assessment of carbon-, biomaterial- and inorganic-based adsorbents for the removal of the most hazardous heavy metal ions from wastewater, RSC Adv. 14 (2024) 11284–11310, https://doi.org/10.1039/D4RA00976B.
[34] P.P. Selvam, S. Preethi, P. Basakaralingam, N. Thinakaran, A. Sivasamy, S. Sivanesan, Removal of rhodamine B from aqueous solution by adsorption onto sodium montmorillonite, J. Hazard. Mater. 155 (2008) 39–44, https://doi.org/10.1016/j.jhazmat.2007.11.025.
[35] T.O. Ajiboye, O.A. Oyewo, D.C. Onwudiwe, Adsorption and photocatalytic removal of Rhodamine B from wastewater using carbon-based materials, FlatChem 29 (2021) 100277, https://doi.org/10.1016/j.flatc.2021.100277.
[36] M.R. Mahmoud, G.M. Rashad, A.M. Elewa, E. Metwally, E.A. Saad, Optimization of adsorption parameters for removal of $^{152+154}Eu$(III) from aqueous solutions by using Zn-Cu-Ni ternary mixed oxide, J. Mol. Liq. 291 (2019) 111257, https://doi.org/10.1016/j.molliq.2019.111257.
[37] A. Varghese, K.R. S.D, D. Pinheiro, Adsorptive removal studies of Rhodamine B by PEG capped polyaniline/$TiO_2$/CuO composite, Mater. Today Commun. 35 (2023) 105739, https://doi.org/10.1016/j.mtcomm.2023.105739.
[38] L. Peng, P. Qin, M. Lei, Q. Zeng, H. Song, J. Yang, J. Shao, B. Liao, J. Gu, Modifying $Fe_3O_4$ nanoparticles with humic acid for removal of Rhodamine B in water, J. Hazard. Mater. 209 (2012) 193–198, https://doi.org/10.1016/j.jhazmat.2012.01.011.
[39] X. Zhao, D. Wang, C. Xiang, F. Zhang, L. Liu, X. Zhou, H. Zhang, Facile synthesis of boron organic polymers for efficient removal and separation of methylene blue, rhodamine B, and rhodamine 6G, ACS Sustain. Chem. Eng. 6 (2018) 16777–16787, https://doi.org/10.1021/acssuschemeng.8b04049.
[40] G. Liao, W. Zhao, Q. Li, Q. Pang, Z. Xu, Novel Poly(acrylic acid)-modified Tourmaline/Silver Composites for Adsorption Removal of Cu(II) ions and Catalytic Reduction of Methylene Blue in Water, Chem. Lett. 46 (2017) 1631–1634, https://doi.org/10.1246/cl.170785.
[41] Z. Yan, T. Wu, G. Fang, M. Ran, K. Shen, G. Liao, Self-assembly preparation of lignin–graphene oxide composite nanospheres for highly efficient Cr(vi) removal, RSC Adv. 11 (2021) 4713–4722, https://doi.org/10.1039/D0RA09190A.
[42] Y. Qiao, C. Sun, J. Jian, T. Zhou, X. Xue, J. Shi, G. Che, G. Liao, Efficient removal of organic pollution via photocatalytic degradation over a $TiO_2$@HKUST-1 yolk-shell nanoreactor, J. Mol. Liq. 385 (2023) 122383, https://doi.org/10.1016/j.molliq.2023.122383.
[43] H. Zhu, C. Zhang, K. Xie, X. Li, G. Liao, Photocatalytic degradation of organic pollutants over $MoS_2$/Ag-$ZnFe_2O_4$ Z-scheme heterojunction: revealing the synergistic effects of exposed crystal facets, defect engineering, and Z-scheme mechanism, Chem. Eng. J. 453 (2023) 139775, https://doi.org/10.1016/j.cej.2022.139775.
[44] C. Li, H. Lu, G. Ding, Q. Li, G. Liao, Recent advances on g-$C_3N_4$-based Z-scheme photocatalysts for organic pollutant removal, Catal. Sci. Technol. 13 (2023) 2877–2898, https://doi.org/10.1039/D3CY00242J.
[45] G. Liao, L. Zhong, C.S. Cheung, C. Du, J. Wu, W. Du, H. Zheng, H. Gao, Direct synthesis of hypercrosslinked microporous poly(para-methoxystyrene) for removal of iron(III) ion from aqueous solution, Microporous Mesoporous Mater. 307 (2020) 110469, https://doi.org/10.1016/j.micromeso.2020.110469.
[46] H. Singh, S. Raj, R.K.S. Rathour, J. Bhattacharya, Bimetallic Fe/Al-MOF for the adsorptive removal of multiple dyes: optimization and modeling of batch and hybrid adsorbent-river sand column study and its application in textile industry wastewater, Environ. Sci. Pollut. Res. 29 (2022) 56249–56264, https://doi.org/10.21203/rs.3.rs-1128193/v1.
[47] K.N. Khattak, M. Zhang, C. Deng, S. Li, L. Jiang, P.G. Karmaker, X. Yang, Fabrication of the $NH_2$-MIL-125(Ti)@TpPa-$NO_2$ hybrid material and its efficient adsorption and removal of rhodamine B in wastewater, Mater. Sci. Eng. B 307 (2024) 117492, https://doi.org/10.1016/j.mseb.2024.117492.
[48] K.M.V. Nguyen, A.V.N. Phan, N.T. Dang, T.Q. Tran, H.K. Duong, H.N. Nguyen, M. V. Nguyen, Efficiently improving the adsorption capacity of the Rhodamine B dye in a $SO_3H$-functionalized chromium-based metal–organic framework, Mater. Adv. 4 (2023) 2636–2647, https://doi.org/10.1039/d3ma00123g.
[49] M.B. Asif, S. Kim, T.S. Nguyen, J. Mahmood, C.T. Yavuz, Covalent organic framework membranes and water treatment, J. Am. Chem. Soc. 146 (2024) 3567–3584, https://doi.org/10.1021/jacs.3c10832.
[50] V.D. da Silva, K. Zalewska, Z. Petrovski, C.D. Buarque, L.C. Branco, P.M. Esteves, Covalent organic frameworks as promising materials for the removal of metal and organic pollutants from water, Mater. Today Sustain 21 (2023) 100279, https://doi.org/10.1016/j.mtsust.2022.100279.
[51] B. Reis, N. Gerlach, K. Pfefferkorn, D. Schwarz, S. Schwarz, Conjugated microporous polymer chitosan hybrid materials for enhanced pollutant removal, Colloids Surf. A Physicochem. Eng. 687 (2024) 133432, https://doi.org/10.1016/j.colsurfa.2024.133432.
[52] Y. Guo, Q.-M. Hasi, J. Yu, Y. Guo, L. Song, S. Wu, X. Luo, L. Chen, Carboxymethyl cellulose/sulfonated conjugated microporous polymer composite aerogel for efficient pollution removal and water evaporation, Sep. Purif. Technol. 324 (2023) 124518, https://doi.org/10.1016/j.seppur.2023.124518.
[53] M.G. Mohamed, M.-Y. Tsai, C.-F. Wang, C.-F. Huang, M. Danko, L. Dai, T. Chen, S.-W. Kuo, Multifunctional polyhedral oligomeric silsesquioxane (POSS) based hybrid porous materials for $CO_2$ uptake and iodine adsorption, Polymers 13 (2021) 221, https://doi.org/10.3390/polym13020221.
[54] M.G. Mohamed, A.F.M. EL-Mahdy, T.-S. Meng, M.M. Samy, S.-W. Kuo, Multifunctional hypercrosslinked porous organic polymers based on tetraphenylethene and triphenylamine derivatives for high-performance dye adsorption and supercapacitor, Polymers 12 (2020) 2426, https://doi.org/10.3390/polym12102426.
[55] Y.J. Zhang, J.Z. Cheng, Y.Q. Xing, Z.R. Tan, G. Liao, S.Y. Liu, Solvent-exfoliated D-A π-polymer @ ZnS heterojunction for efficient photocatalytic hydrogen evolution, Mater. Sci. Semicond. Proc. 161 (2023) 107463, https://doi.org/10.1016/j.mssp.2023.107463.
[56] Z.Q. Shen, G. Zhang, K. Yang, Y.J. Zhang, H. Gong, G. Liao, S.Y. Liu, Direct C–H arylation derived ternary D–A conjugated polymers: effects of monomer geometries, D/A ratios, and alkyl side chains on photocatalytic hydrogen

production and pollutant degradation, Macromol. Rapid Commun. 45 (2024) 2300566, https://doi.org/10.1002/marc.202300566.
[57] Z.R. Tan, Y.Q. Xing, J.Z. Cheng, G. Zhang, Z.Q. Shen, Y.J. Zhang, G. Liao, L. Chen, S.Y. Liu, EDOT-based conjugated polymers accessed via C–H direct arylation for efficient photocatalytic hydrogen production, Chem. Sci. 13 (2022) 1725–1733, https://doi.org/10.1039/D1SC05784G.
[58] J.Z. Cheng, L.L. Liu, G. Liao, Z.Q. Shen, Z.R. Tan, Y.Q. Xing, X.X. Li, K. Yang, L. Chen, S.Y. Liu, Achieving an unprecedented hydrogen evolution rate by solvent-exfoliated CPP-based photocatalysts, J. Mater. Chem. A 8 (2020) 5890–5899, https://doi.org/10.1039/C9TA13514F.
[59] T.H. Weng, M.G. Mohamed, S.U. Sharma, S.V. Chaganti, M.M. Samy, J.T. Lee, S. W. Kuo, Ultrastable three-dimensional triptycene- and tetraphenylethene-conjugated microporous polymers for energy storage, ACS Appl. Energy Mater. 5 (2022) 14239–14249, https://doi.org/10.1021/acsaem.2c02809.
[60] M.G. Mohamed, S.U. Sharma, C.H. Yang, M.M. Samy, A.A.K. Mohammed, S. V. Chaganti, J.T. Lee, S.W. Kuo, Anthraquinone-enriched conjugated microporous polymers as organic cathode materials for high-performance lithium-ion batteries, ACS Appl. Energy Mater. 4 (2021) 14628–14639, https://doi.org/10.1021/acsaem.1c03270.
[61] M.M. Samy, M.G. Mohamed, S.U. Sharma, S.V. Chaganti, J.T. Lee, S.W. Kuo, An ultrastable tetrabenzonaphthalene-linked conjugated microporous polymer functioning as a high-performance electrode for supercapacitors, J. Taiwan Inst. Chem. Eng. (2023) 104750, https://doi.org/10.1016/j.jtice.2023.104750.
[62] S.Y. Chang, A.M. Elewa, M.G. Mohamed, I.M.A. Mekhemer, M.M. Samy, K. Zhang, H.H. Chou, S.W. Kuo, Rational design and synthesis of bifunctional Dibenzo [g,p] chrysene-based conjugated microporous polymers for energy storage and visible light-driven photocatalytic hydrogen evolution, Mater. Today Chem. 33 (2023) 101680, https://doi.org/10.1016/j.mtchem.2023.101680.
[63] A.O. Mousa, C.H. Chuang, S.W. Kuo, M.G. Mohamed, Strategic design and synthesis of ferrocene linked porous organic frameworks toward tunable $CO_2$ capture and energy storage, Int. J. Mol. Sci. 24 (2023) 12371, https://doi.org/10.3390/ijms241512371.
[64] M.G. Mohamed, M.G. Kotp, A.O. Mousa, Y.S. Li, S.W. Kuo, Construction of Fe- and N-doped microporous carbon from ferrocene-based conjugated microporous polymers for supercapacitive energy storage, ACS Appl. Energy Mater. 8 (2025) 2389–2402, https://doi.org/10.1021/acsaem.4c02968.
[65] A. Basit, M.G. Mohamed, S.U. Sharma, S.W. Kuo, Thianthrene- and thianthrene tetraoxide-functionalized conjugated microporous polymers for efficient energy storage, ACS Appl. Polym. Mater. 6 (2024) 12247–12260, https://doi.org/10.1021/acsapm.4c02368.
[66] M.G. Mohamed, A.F.M. EL-Mahdy, M.G. Kotp, S.W. Kuo, Advances in porous organic polymers: syntheses, structures, and diverse applications, Mater. Adv. 3 (2022) 707–733, https://doi.org/10.1039/D1MA00771H.
[67] J.S.M. Lee, A.I. Cooper, Advances in conjugated microporous polymers, Chem. Rev. 120 (2020) 2171–2214, https://doi.org/10.1021/acs.chemrev.9b00399.
[68] Y. Xu, S. Jin, H. Xu, A. Nagai, D. Jiang, Conjugated microporous polymers: design, synthesis and application, Chem. Soc. Rev. 42 (2013) 8012–8031, https://doi.org/10.1039/c3cs60160a.
[69] M.G. Mohamed, S.U. Sharma, P.T. Wang, M. Ibrahim, M.H. Lin, C.L. Liu, M. Ejaz, H.J. Yen, S.W. Kuo, Construction of fully π-conjugated, diyne-linked conjugated microporous polymers based on tetraphenylethene and dibenzo [g, p] chrysene Units for energy storage, Polym. Chem. 15 (2024) 2827–2839, https://doi.org/10.1039/D4PY00421C.
[70] A.O. Mousa, Z.I. Lin, S.V. Chaganti, C.H. Chuang, C.K. Chen, S.W. Kuo, M. G. Mohamed, Bifunctional imidazolium linked tetraphenylethene based conjugated microporous polymers for dynamic antibacterial properties and supercapacitor electrodes, Polym. Chem. 15 (2024) 397–411, https://doi.org/10.1039/D3PY01303K.
[71] M.G. Mohamed, C.C. Chen, M. Ibrahim, A.O. Mousa, M.H. Elsayed, Y. Ye, S.W. Kuo, Tetraphenylanthraquinone and dihydroxybenzene-tethered conjugated microporous polymer for enhanced $CO_2$ uptake and supercapacitive energy storage, JACS Au 4 (2024) 3593–3605, https://doi.org/10.1021/jacsau.4c00537.
[72] S.U. Sharma, M.H. Elsayed, I.M.A. Mekhemer, T.S. Meng, H.H. Chou, S.W. Kuo, M. G. Mohamed, Rational design of pyrene and thienyltriazine-based conjugated microporous polymers for high-performance energy storage and visible-light photocatalytic hydrogen evolution from water, Giant 17 (2024) 100217, https://doi.org/10.1016/j.giant.2023.100217.
[73] M.G. Mohamed, M. Ibrahim, N.P. Chen, A. Basit, Y.C. Kao, A.O. Mousa, M. M. Samy, S.W. Kuo, Tetrabenzonaphthalene and redox-active anthraquinone-linked conjugated microporous polymers as organic electrodes for enhanced energy storage efficiency, ACS Appl. Energy Mater. 7 (2024) 5582–5593, https://doi.org/10.1021/acsaem.4c01276.
[74] S. Gharbi, N. Méndez-Gil, K. Hriz, M. Majdoub, B. Gómez-Lor, Truxene-based porous triazole-linked polymers for dye removal through synergetic adsorption and photodegradation, ACS Appl. Polym. Mater. 5 (2023) 2359–2366, https://doi.org/10.1021/acsapm.2c02033.
[75] J. Yin, Y. Ren, X. Sun, Y. Gao, Z. Tian, D. Li, Thiazolo[5,4-d]thiazole-based covalent organic frameworks for the rapid removal of RhB, Catalysts 15 (2025) 42, https://doi.org/10.3390/catal15010042.
[76] S. Wang, X. Meng, H. Luo, L. Yao, X. Song, Z. Liang, Post-synthetic modification of conjugated microporous polymer with imidazolium for highly efficient anionic dyes removal from water, Sep. Purif. Technol. 284 (2022) 120245, https://doi.org/10.1016/j.seppur.2021.120245.
[77] M.G. Mohamed, C.C. Chen, S.W. Kuo, Nitrogen and sulfur co-doped microporous carbon through benzo[c]-1,2,5-thiadiazole-functionalized benzoxazine-linkage porous organic polymer in $CO_2$ capture and energy storage, React. Funct. Polym. 214 (2025) 106286, https://doi.org/10.1016/j.reactfunctpolym.2025.106286.
[78] M.G. Mohamed, W.C. Chang, S.W. Kuo, Crown ether- and benzoxazine-linked porous organic polymers displaying enhanced metal ion and $CO_2$ capture through solid-state chemical transformation, Macromolecules 55 (2022) 7879–7892, https://doi.org/10.1021/acs.macromol.2c01216.
[79] M.G. Mohamed, T.C. Chen, S.W. Kuo, Solid-state chemical transformations to enhance gas capture in benzoxazine-linked conjugated microporous polymers, Macromolecules 54 (2021) 5866–5877, https://doi.org/10.1021/acs.macromol.1c00736.
[80] M.G. Mohamed, B.X. Su, S.W. Kuo, Robust nitrogen-doped microporous carbon via crown ether-functionalized benzoxazine-linked porous organic polymers for enhanced $CO_2$ adsorption and supercapacitor applications, ACS Appl. Mater. Interfaces 16 (2024) 40858–40872, https://doi.org/10.1021/acsami.4c05645.
[81] G.M. Rashad, M.R. Mahmoud, A.M. Elewa, E. Metwally, E.A. Saad, Removal of radiocobalt from aqueous solutions by adsorption onto low-cost adsorbents, J. Radioanal. Nucl. Chem. 309 (2016) 1065–1076, https://doi.org/10.1007/s10967-016-4726-4.
[82] A.S.M.G. El-hak, A.A.K. Mohammed, A.F.A. Hakiem, R.M. Mahfouz, Molecular conformation, vibrational spectroscopic and NBO analysis of atenolol and atenolol-hydrochlorothiazide cocrystals, Spectrochim. Acta Part A (2019) 117200, https://doi.org/10.1016/j.saa.2019.117200.
[83] R.G. Parr, R.G. Pearson, Absolute hardness: companion parameter to absolute electronegativity, J. Am. Chem. Soc. 105 (1983) 7512, https://doi.org/10.1021/ja00364a005.